RSC Advances

PAPER

View Article Online
View Journal | View Issue

Cite this: *RSC Adv.*, 2025, **15**, 47803

Enhancement of stability and electronic properties of ultra-high nickel cathodes by aluminium and boron codoping studied by combined density functional theory and neural network models

Nguyen Vo Anh Duy,[ab] Tran Van Thien,†[ac] Nguyen Thi Bao Trang,[ab] Nguyen Huu Phuc,[a] To Van Nguyen,[d] Truong Minh Thai,[a] Yoshiyuki Kawazoe[efg] and Minh Triet Dang *[a]

The rapid growth of electric vehicles and large-scale energy storage systems has intensified research on nickel-rich lithium-ion battery cathodes, prized for their high energy density, superior electrochemical performance, and reduced material costs. In this study, density functional theory (DFT) calculations are integrated with machine learning (ML) techniques using DeePMD-based neural network models to investigate the structural stability and electronic properties of Ni-rich cathode materials, including $LiNi_{0.6}Mn_{0.2}Co_{0.2}O_2$ (NMC622), $LiNi_{0.8}Mn_{0.1}Co_{0.1}O_2$ (NMC811), and $LiNi_{0.9}Co_{0.05}Mn_{0.05}O_2$ (NMC955). The neural network models successfully reproduce DFT-calculated energies and forces with R^2 values exceeding 0.9, enabling accurate prediction of thermodynamic stability across wide temperature ranges. Increasing Ni content enhances electronic conductivity but reduces structural robustness due to intensified Ni–O hybridization. Co-doping NMC955 with aluminum and boron improves lattice stability, redistributes charge, and lowers the Li-ion diffusion barrier from 0.355 eV to 0.206 eV. Thus, Al–B co-doping achieves a favorable balance between electronic and structural performance. This integrated DFT-ML framework offers an efficient pathway for the rational design of robust, high-energy Ni-rich cathodes for next-generation lithium-ion batteries.

Received 19th May 2025
Accepted 12th November 2025

DOI: 10.1039/d5ra03510d

rsc.li/rsc-advances

1. Introduction

The global demand for energy production and storage has steadily increased in recent years. Lithium-ion batteries (LIBs) have become indispensable to the advancement of portable electronics, electric vehicles, and large-scale energy storage systems.[1,2] Conventional LIBs, typically employing $LiCoO_2$ cathodes and graphite anodes, face scalability challenges due to the scarcity and high extraction cost of lithium.[3] These limitations have motivated extensive research into alternative cathode materials. Efforts have focused on enhancing energy density, structural stability, and cycling performance through material modification and compositional tuning. Representative cathode materials include metal oxides such as MnO_2,[4] MoO_3,[5] Prussian blue derivatives,[6] honeycomb-layered oxides like $A_2Ni_2TeO_6$ (A = Na, K),[7] and layered transition-metal oxides. Among them, layered NMC oxides (NMC, $LiNi_xMn_yCo_zO_2$, $x + y + z = 1$) have emerged as leading candidates for next-generation LIBs. NMC materials combine the advantages of their constituent elements, offering high discharge capacity, long cycle life, and excellent thermal and rate performance.[8] Various compositions have been developed, including $LiNi_{1/3}Mn_{1/3}Co_{1/3}O_2$ (NMC333),[9] $LiNi_{0.5}Mn_{0.3}Co_{0.2}O_2$ (NMC532),[10,11] $LiNi_{0.6}Mn_{0.2}Co_{0.2}O_2$ (NMC622),[12,13] $LiNi_{0.8}Mn_{0.1}Co_{0.1}O_2$ (NMC811),[14,15] and more recently, $LiNi_{0.9}Co_{0.05}Mn_{0.05}O_2$ (NMC955).[16,17] The cost of NMC cathodes is largely determined by their nickel content. Increasing Ni concentration reduces cost, since nickel precursors are abundant, and enhances charge-storage capacity. Manganese contributes to thermal stability, while cobalt improves structural robustness.[18] For example, NMC622 delivers an initial discharge capacity of 190.5 mAh g^{-1} with a coulombic efficiency of 78.7%, retaining 74.9% of its capacity after 100 cycles with nearly 100% coulombic efficiency.[19] NMC811 achieves over 200 mAh g^{-1}, a specific energy exceeding

[a]*Can Tho University, 3-2 Road, Can Tho City 900000, Vietnam. E-mail: dmtriet@ctu.edu.vn*
[b]*FPT University, Can Tho Campus, 600 Nguyen Van Cu Street, Can Tho, Ninh Kieu 900000, Vietnam*
[c]*Dak Nong Community College, Hung Vuong Street, Dak Nong, 640000, Vietnam*
[d]*Faculty of Chemical-Physical Engineering, Le Quy Don Technical University, Ha Noi 100000, Vietnam*
[e]*New Industry Creation Hatchery Center (NICHe), Tohoku University, Sendai, Japan*
[f]*Department of Physics, SRM University-AP, Amaravati 522240, Andhra Pradesh, India*
[g]*School of Physics, Institute of Science and Center of Excellence in Advanced Functional Materials, Suranaree University of Technology, Nakhon Ratchasima 30000, Thailand*
† These authors contribute equally.

600 Wh kg^{-1}, and excellent rate capability, supported by its high electrical conductivity ($\sim 2.8 \times 10^{-5}$ S cm^{-1}) and Li^+ diffusion coefficient (10^{-8} to 10^{-9} cm^2 s^{-1}).[20] NMC955 is predicted to reach 227 mAh g^{-1} at a 4.3 V cutoff;[17] however, it suffers from rapid capacity fading, retaining only 87% and 81% of its initial capacity after 100 cycles at 4.3 V and 4.5 V, respectively. This degradation stems from structural instabilities in Ni-rich electrodes, where abrupt lattice distortions generate local stress, microcracks, and anisotropic deformations during cycling.[17,21,22] These effects compromise mechanical integrity and shorten cathode lifespan.[23] To overcome these challenges, extensive efforts have been devoted to improving the mechanical strength, capacity retention, rate performance, and high-voltage stability of Ni-rich NMCs.[24–27]

Doping has proven particularly effective in stabilizing such materials.[28–30] Incorporating mono- or multivalent cations enhances the structural integrity of Ni-rich cathodes by stabilizing the electrode surface, minimizing cation disorder, suppressing oxygen release, and reducing interfacial stress. In addition to high-valence dopants, small-radius cations such as Ag^+, Al^{3+}, B^{3+}, Ti^{4+}, Zr^{4+}, and Mo^{6+} have shown significant benefits in improving the electrochemical performance of both Ni-rich and Li-/Mn-rich cathodes. For example, boron doping markedly enhances capacity retention compared with undoped counterparts,[31,32] while aluminum doping effectively mitigates structural degradation and capacity fading.[33] Specifically, Al^{3+} ions reduce Ni oxidation-state disorder and suppress Li^+/Ni^{2+} cation mixing. Al-doped NMC cathodes exhibit excellent cycling stability, retaining 70% of their capacity after 1000 cycles at a high rate of 10C.[34] Moreover, Al^{3+} can form a protective interfacial layer between the electrode and electrolyte, suppressing cation dissolution and further enhancing long-term stability.[35,36]

To evaluate and optimize cathode stability, machine learning (ML) has emerged as a powerful tool that complements traditional first-principles approaches. ML models, particularly deep neural networks, can predict energy landscapes and atomic forces with near-DFT accuracy at a fraction of the computational cost.[37] The Deep Potential (DP) method, for instance, preserves the symmetry and locality of atomic interactions while enabling large-scale simulations of phase transitions and thermal effects in complex materials.[38] The integration of ML with DFT is thus transforming battery materials research, providing predictive insights into degradation mechanisms and accelerating the design of robust, high-energy cathodes.

In this study, we investigated the structural stability of Ni-rich NMC cathodes at elevated temperatures to identify the most stable composition among NMC622, NMC811, and NMC955. A machine learning framework was developed to compare DFT-calculated properties with ML-predicted values using deep neural networks trained on DFT-derived energies and atomic forces. Our results indicate that NMC955 exhibits the highest intrinsic structural stability. To further enhance its performance, we explored co-doping strategies with aluminum (Al) and boron (B) to examine their effects on the electronic structure. Co-doping with Al and B significantly improved both structural integrity and electronic stability, demonstrating the potential of this approach to optimize Ni-rich cathodes. These findings highlight the effectiveness of combining DFT and ML methods to accelerate the discovery of next-generation lithium-ion battery materials and guide the rational design of stable, high-performance cathodes.

2. Computational details

2.1 Machine-learning background

The machine learning approach integrates DFT with Deep Potential Molecular Dynamics (DeePMD) methods to predict and optimize the performance of nickel-rich cathode materials for lithium-ion batteries. The implemented neural network architecture is a Residual Network (ResNet), which maps atomic coordinates to energy predictions.[39] The computational model formulates the energy function by fitting neural network parameters and summing the energies of local atomic environments. An encoding network encodes the atomic environments into a descriptor space, which maintains physical symmetry by employing two-body embedding DeepPot-SE descriptors.[40] This descriptor space is then processed by a ResNet fitting network to predict energies. The model is trained using a loss function based on mean squared error (MSE) for both energy and force predictions, optimized through the Adam optimizer with a decaying learning rate.[41] Training data is generated from DFT simulations conducted with the VASP software package, with energies, forces, and atomic coordinates extracted using the *dpdata* library. Hyperparameter settings include three-layer ResNet architectures for encoding and fitting networks, hyperbolic tangent activation functions, and a cutoff radius of 6.0 Å. The training involves 30 000 steps with automatic batch size adjustments to ensure robust model convergence. A similar successful approach was employed for predicting the topological structural stability of twisted hexagonal boron nitride heterostructures.[42] In this work, the DeePMD model was developed and rigorously validated against DFT energy-force data to ensure an accurate potential energy surface, establishing a solid foundation for future large-scale molecular dynamics simulations of Ni-rich NMC cathodes. For more details, please refer to the SI.

To generate the training and validation datasets, *ab initio* molecular dynamics (AIMD) trajectories were performed in the NVT ensemble using the Nose thermostat for each composition. Each trajectory comprised 500 ionic steps with a 3 femtosecond time step, corresponding to a total simulation time of approximately 1.5 ps. The per-atom energies and forces from all configurations were collected, with 80% of the frames randomly assigned to the training set and 20% retained for independent validation using the dpdata package.

2.2 Density functional theory approach

All DFT simulations are performed using the Projector Augmented Wave (PAW) method implemented in the Vienna *Ab initio* Simulation Package (VASP).[43–45] For ionic relaxations, we used the generalized gradient approximation of the Perdew–

Burke–Ernzerhof for solids (PBESol)[46,47] as an exchange-correlation functional. The convergence threshold for the self-consistent field calculations was set to 10^{-4} eV per cell, and the geometrical structures were fully optimized until the Hellmann–Feynman forces acting on atoms were less than 0.005 eV $Å^{-1}$.[48]

To accurately describe the density of states for the investigated cathode materials, we enhance our DFT calculations by incorporating Hubbard U corrections to address the self-interaction error associated with the d orbitals of transition metals. The applied Hubbard U values are 6 eV for Ni, 6 eV for Co, and 4.5 eV for Mn, as suggested in ref. 48. Additionally, an energy cutoff of 600 eV ensures good convergence of the total energy. The integration in the Brillouin zone is employed using the Monkhorst–Pack scheme[49] $(2 \times 3 \times 1)$, $(4 \times 4 \times 1)$, $(3 \times 5 \times 2)$ for NMC622, NMC811, and NMC955, respectively.

The charge–discharge behavior serves as a critical indicator of the performance and applicability of Ni-rich NMC cathodes in lithium-ion batteries. To evaluate lithium-ion migration, the climbing-image nudged elastic band (NEB) method,[50,51] implemented in the AMS package was utilized. The optimized initial and final structures were used to define each migration pathway, which was interpolated through nineteen intermediate images along the NEB trajectory. The diffusion coefficient of lithium ions can be calculated *via*[52,53] $D = a^2 \nu e^{-\frac{E_{act}}{k_B T}}$, where a is the diffusion length of ions, $\nu \sim 10^{13}$ Hz, k_B Boltzmann's constant, T the room temperature ($T = 300$ K), and E_{act} the diffusion barrier.

3. Results and discussion

3.1 Thermal stability of Ni-rich NMC cathode materials

Fig. 1 illustrates the optimized configurations of NMC622, NMC811, and NMC955. All configurations exhibit the typical hexagonal lattice structure ($R\bar{3}m$ space group) of $LiNiO_2$,[54,55] with a total number of atoms in the models being 120, 96, and 96, respectively. Manganese and cobalt atoms are substituted at nickel sites in the transition metal layer to enhance the performance, structural stability, and cost-effectiveness of NMC materials.[48] The corresponding lattice parameters in Table 1 agree well with the results reported in ref. 13, 15 and 17, confirming the reliability of these configurations for further investigation.

During the charge/discharge process of lithium-ion batteries, cathode materials undergo thermal fluctuations driven by electrochemical reactions and electronic transport. The thermodynamic stability of these cathode materials is a critical factor in determining their ability to retain structural integrity, suppress undesirable side reactions, and mitigate the risk of thermal runaway. To investigate these aspects, this study evaluates the thermal stability of NMC cathode systems at four benchmark temperatures: 27 °C (ambient), 750 °C, 950 °C, and 1650 °C (Fig. 2). Room temperature (27 °C) represents typical operating conditions, while the elevated temperatures were carefully selected to simulate increasingly extreme thermal environments that can arise during battery abuse or in thermal processing. Specifically, 750 °C and 950 °C represent common synthesis or sintering temperatures for NMC materials, providing insight into stability during manufacturing and moderate thermal stress. The inclusion of 1650 °C, which exceeds conventional stability testing thresholds, serves as an extreme condition to probe the ultimate structural stability of these materials near the melting point, as thoroughly studied in ref. 56. Thus, these selected temperature points allow for a comprehensive understanding of how structural integrity evolves under realistic and severe thermal conditions. The optimized structures of NMC622, NMC811, and NMC955 at each temperature were obtained from *ab initio* molecular dynamics (AIMD) simulations in the NVT ensemble with a Nosé thermostat. Each simulation ran for 500 ionic steps with a 3 femtosecond time step, yielding a total duration of ~1.5 ps, an appropriate timescale given the high computational cost of these systems.[57] The final atomic configuration of each trajectory was used as the representative quasi-equilibrium structure for subsequent structural and XRD analyses. This approach ensures that the systems reach a quasi-equilibrated state at the target temperature (see Fig. S1). Fig. 2 shows the temperature-dependent structural evolution of NMC622, NMC811, and NMC955, and Fig. 3 presents the corresponding XRD patterns, both obtained from the configurations after 500 simulation steps. Longer simulations could yield additional structural rearrangements. At 27 °C, all compositions exhibit the typical layered $LiNiO_2$-type structure with alternating Li and transition-metal (TM) oxide slabs.[54,55] Upon heating to 750–950 °C, local cation rearrangements occur, including Ni migration from the TM to the Li layers and partial Li/Ni disorder. This effect is more

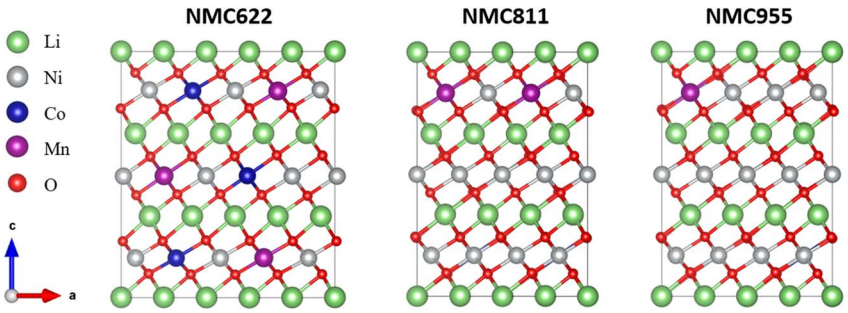

Fig. 1 Side views of the fully lithiated NMC622, NMC811, and NMC955 cathode materials. Green, gray, purple, blue, and red spheres represent lithium, nickel, manganese, cobalt, and oxygen atoms, respectively.

Table 1 Lattice parameters of the fully lithiated NMC cathode materials. Lattice parameters of ref. 15 and 17 are presented for comparison

Material	a (Å)	c (Å)	c/a
NMC622	2.843 | 2.868 (ref. 17)	14.215 | 14.224 (ref. 17)	5.00 | 4.96 (ref. 17)
NMC811	2.899 | 2.840 (ref. 15)	14.333 | 14.102 (ref. 15)	4.94 | 4.97 (ref. 15)
NMC955	2.912 | 2.874 (ref. 17)	14.332 | 14.205 (ref. 17)	4.92 | 4.94 (ref. 17)

pronounced in Ni-rich compositions (NMC811 and NMC955) due to the similar ionic radii of Ni^{2+} and Li^{+}. At 1650 °C, the layered order collapses, forming a rock-salt-like phase with extensive cation disorder and loss of Li–O-TM stacking. These temperature-driven transformations align with the XRD analyses reported by Schwarz *et al.*,[58] where increasing disorder and strain were observed at high temperature or high Ni fraction, as well as with the degradation mechanisms summarized by Jiang *et al.*,[59] which describe thermally induced phase transitions from layered to spinel and ultimately to rock-salt structures in Ni-rich NMCs. Overall, increasing Ni content promotes cation mixing and accelerates structural reconstruction upon heating, progressively weakening the long-range layered order crucial for reversible Li^{+} intercalation.

Fig. 3 shows the corresponding X-ray diffraction patterns, offering a broader statistical perspective on the temperature-dependent phase evolution of the NMC materials. At room temperature, all samples display sharp, well-defined peaks indicative of high crystallinity and phase purity. When heated to 750 °C and 950 °C, NMC622 retains its layered structure with only minor peak broadening, suggesting good thermal stability. In contrast, NMC811 and, especially, NMC955 exhibit greater peak broadening and a lower (003)/(104) intensity ratio, indicating enhanced Li/Ni cation disorder and partial collapse of the layered framework. At 1650 °C, additional peaks associated with a rock-salt-like phase emerge, confirming a complete loss of long-range ordering. NMC622, however, preserves a partially layered structure with only weak rock-salt features. These observations demonstrate that thermal stability decreases with increasing Ni content, consistent with the weaker Ni–O bond strength and greater susceptibility of Ni-rich compositions to oxygen loss and cation migration at high temperatures. Collectively, the XRD and AIMD results reveal that Ni enrichment destabilizes the layered structure, promoting the irreversible transition from the ordered $R\bar{3}m$ phase to a disordered framework under thermal stress. More interestingly, while the

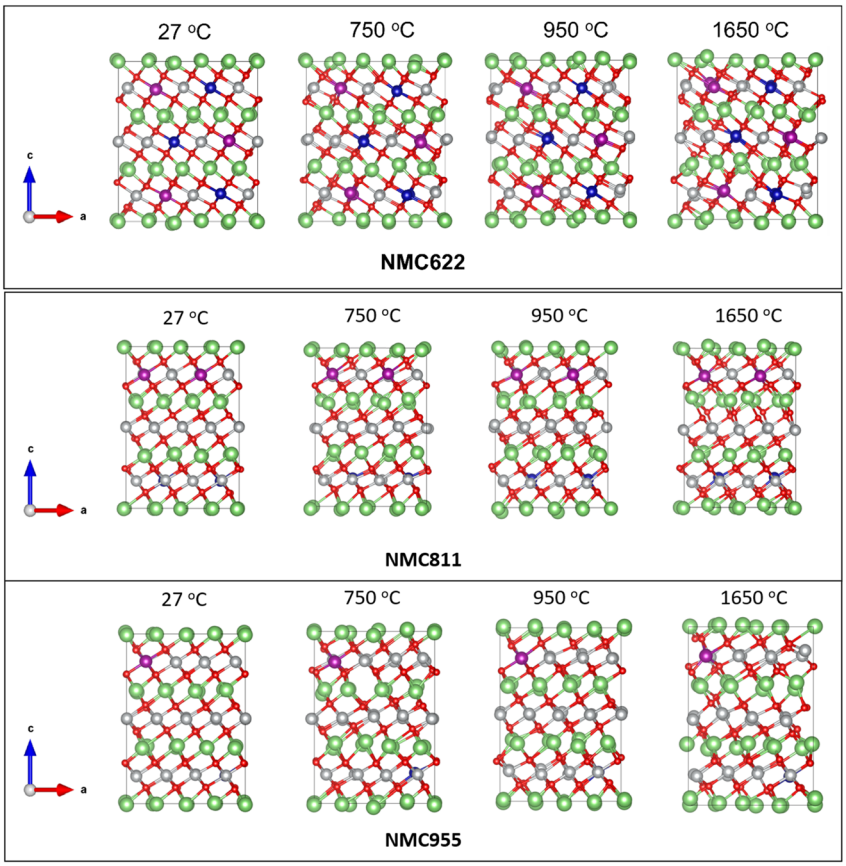

Fig. 2 Side views of the fully lithiated NMC622, NMC811, and NMC955 cathode materials at 27 °C, 750 °C, 950 °C, and 1650 °C, respectively. Green, gray, purple, blue, and red spheres represent lithium, nickel, manganese, cobalt, and oxygen atoms, respectively.

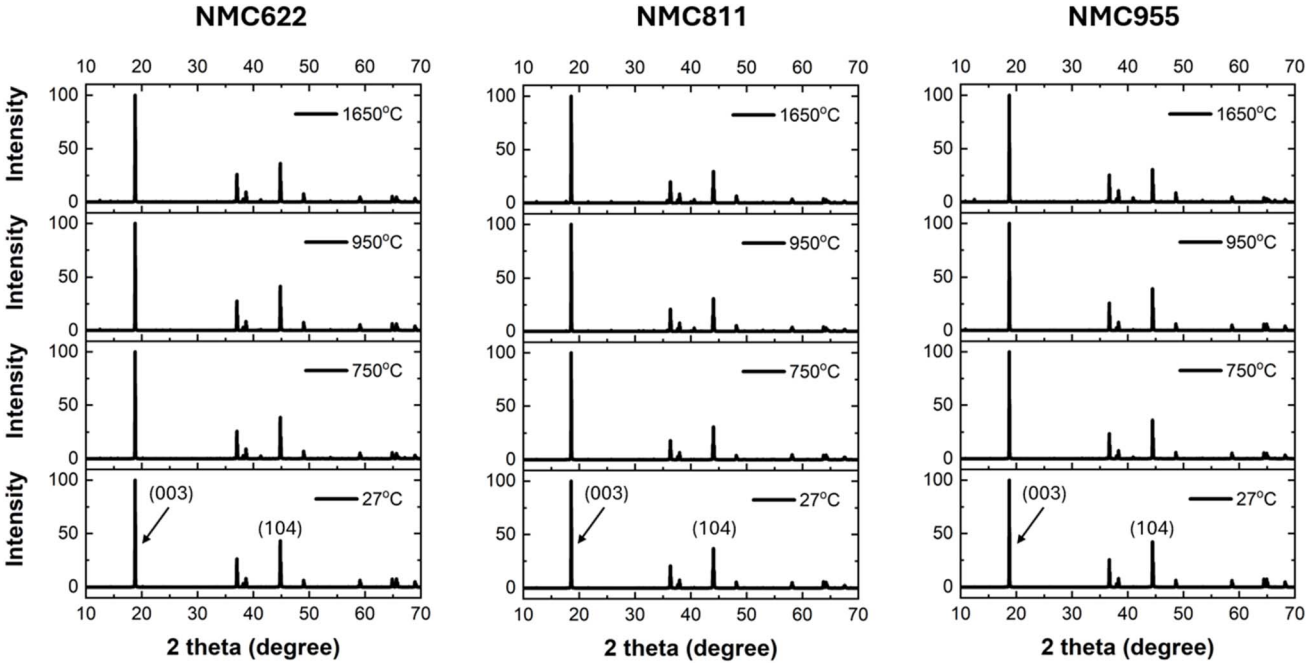

Fig. 3 X-ray diffraction of the fully lithiated NMC622, NMC811, and NMC955 cathode materials at 27 °C, 750 °C, 950 °C, and 1650 °C, respectively.

XRD analysis of the fully lithiated samples established that thermal stability decreases with increasing Ni content, as Ni-rich compositions undergo faster transitions from the layered to rock-salt-like structure upon heating. To further examine the effect of lithium content, Fig. S2 and S3 compare the XRD patterns of partially lithiated NMC622, NMC811, and NMC955. At 27 °C (Fig. S2), all samples retain the layered $R\bar{3}m$ structure, but the (003)/(104) intensity ratio decreases with increasing Ni content and decreasing Li concentration, indicating enhanced Li/Ni cation disorder. At 1650 °C (Fig. S3), this trend becomes more pronounced: NMC622 largely preserves its layered reflections, whereas NMC811 and NMC955 exhibit significant peak merging and the emergence of rock-salt-like features. These results confirm that both Ni enrichment and Li depletion lower structural and thermal stability by promoting oxygen loss and Ni migration. Thus, partially lithiated Ni-rich NMCs are even more susceptible to high-temperature phase transitions than their fully lithiated counterparts.

We further investigate the structural stability of these Ni-rich NMC cathode materials obtained from density functional theory compared to those produced by the Deep Potential Molecular Dynamics model. In Fig. S4, the energies predicted by the DeePMD model closely align with those calculated by DFT, indicating that the DeePMD model is well-trained. The predicted energy values are close to the DFT reference line across selected temperature benchmarks. There is some slight data scattering at 1650 °C; however, this remains minor. The coefficient of determination (R^2) for all models across the four temperature points exceeds 0.9, demonstrating the model's strong ability to reproduce realistic energy values.

DeePMD-predicted forces align closely with DFT results, with data points that accurately match the DFT reference curve in all three spatial directions: x, y, and z. The force ranges (in the unit of eV Å^{-1}) for the materials NMC622, NMC811, and NMC955 are approximately as follows: −2 to 2 at 27 °C, −4 to 4 at both 750 °C and 950 °C, and −6 to 6 at 1650 °C (Fig. 4). In other words, the results at 950 °C and 1650 °C show a wider scattering compared to those at 27 °C and 750 °C. This issue is likely due to increased atomic vibrations at elevated temperatures, which complicate model training. Although the accuracy of force predictions is slightly lower than that of energy predictions, it remains high, generally exceeding 0.9. These findings demonstrate that the DeePMD model effectively predicts the atomic dynamics of NMC systems, achieving over 90% accuracy in energy and force predictions (Table 2).

3.2 Effects of AlB codoping on the electronic properties of Ni-rich NMC cathode materials

Fig. 5 and S5 illustrate the evolution of the electronic structure as the Ni content increases. In all three materials, the valence band below the Fermi level is primarily composed of O-2p and Ni-3d states, with minor contributions from Co-3d and Mn-3d. The substantial overlap between O-2p and Ni-3d orbitals in the −6 to 0 eV range indicates significant Ni–O covalent hybridization, which governs both the redox behavior and the stability of these layered oxides. The conduction band just above the Fermi level is dominated by unoccupied Ni-e_g states, showing that Ni acts as the primary redox center.

As the nickel content increases from NMC622 to NMC811 and then to NMC955, the overall bandwidth of the O-2p and Ni-3d states broadens and their energy separation narrows. In

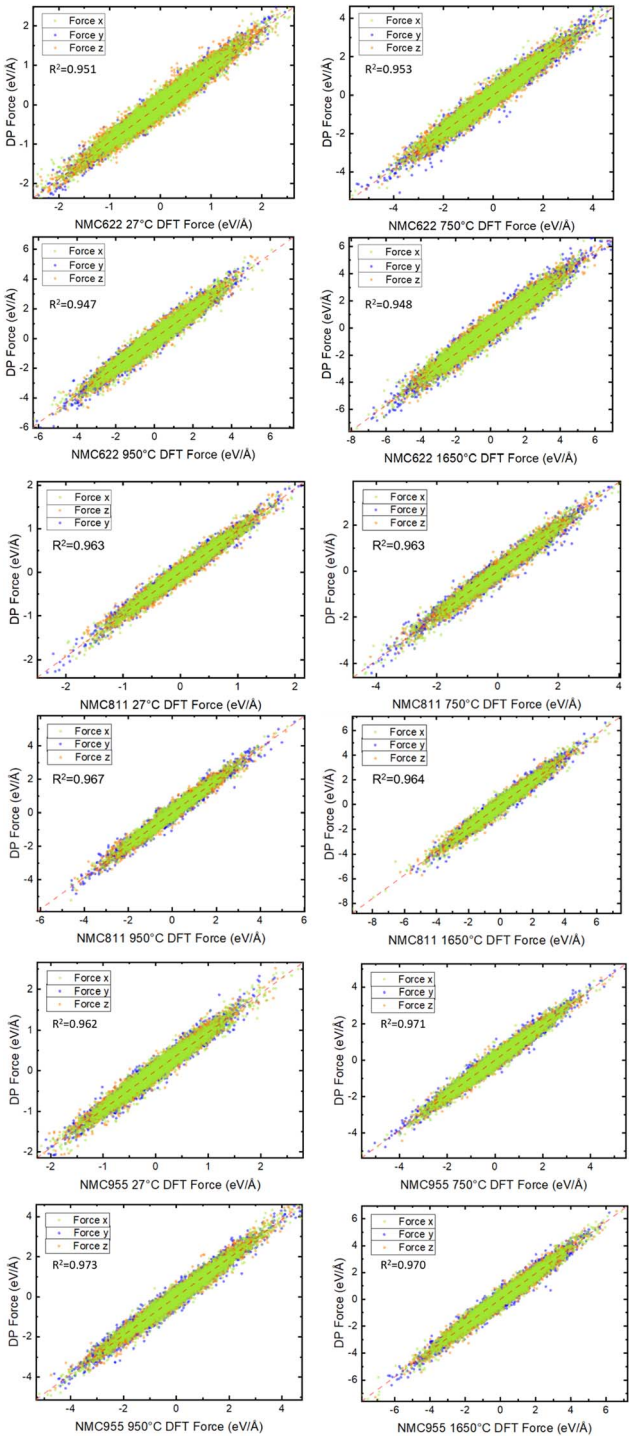

Fig. 4 Comparison of forces of the DeePMD force model with DFT calculations for NMC622, NMC811, and NMC955 cathode materials in the validation dataset.

NMC622, there remains a distinct gap between the O-2p valence and Ni-3d conduction bands, implying moderate covalency and relatively ionic bonding. The Ni-3d states are mainly localized below the Fermi level, while the O-2p orbitals dominate the valence band, indicating that redox activity is largely Ni-centered with limited oxygen participation. As the Ni fraction

Table 2 The coefficient of determination (R^2) of DeePMD models of the energy and forces for NMC622, NMC811, and NMC955 cathode materials at 27 °C, 750 °C, 950 °C, and 1650 °C

Sample	Temperature	R^2 (E)	R^2 (F)
NMC622	27 °C	0.942	0.951
	750 °C	0.988	0.953
	950 °C	0.982	0.947
	1650 °C	0.992	0.948
NMC811	27 °C	0.980	0.963
	750 °C	0.987	0.963
	950 °C	0.986	0.967
	1650 °C	0.973	0.964
NMC955	27 °C	0.991	0.962
	750 °C	0.993	0.971
	950 °C	0.991	0.973
	1650 °C	0.989	0.970

rises to NMC811, the Ni-3d states begin to cross the Fermi level and become the dominant conduction channel. The O-2p states exhibit greater hybridization with the Ni-3d orbitals, extending closer to and slightly above the Fermi level. This enhanced overlap demonstrates increased electronic delocalization and Ni–O covalency, suggesting the emergence of oxygen redox activity at high voltages. Hybridization implies the formation of ligand holes (O-holes) in the O-2p band, a feature characteristic of Ni-rich cathodes. While such oxygen participation can boost capacity, it also introduces a risk of oxygen instability and lattice degradation. Meanwhile, cobalt and manganese remain largely redox-inactive across these compositions, serving primarily as structural stabilizers, consistent with previous computational and experimental findings.[15,21,22]

In NMC955, the degree of hybridization reaches its maximum: the O-2p states shift further upward, nearly merging with the Ni-3d band, and the Fermi level cuts directly through these hybridized states. This near-vanishing separation between O-2p and Ni-3d bands reveals a highly metallic, delocalized electronic structure and a substantial increase in electronic conductivity. The density of Ni-3d states at the Fermi level is significantly higher, enabling efficient charge transport but also indicating a strong tendency toward oxygen redox participation. The O-2p orbitals extend well into the conduction region. However, this same behavior correlates with greater structural and thermal instability, as enhanced Ni–O covalency weakens oxygen binding and promotes O_2 evolution. The Co and Mn 3d states remain electronically inert throughout, consistent with their stabilizing, non-redox-active roles. Although NMC955 exhibits the highest electronic conductivity and Ni-centered redox activity, it is the most prone to oxygen-related degradation. By contrast, NMC811 achieves a balance between conductivity and structural integrity, which explains its prominence in commercial applications, whereas NMC622, though more stable, requires conductive additives to perform effectively in high-power systems.

These trends align closely with previous theoretical and computational studies. Dixit *et al.*[60] showed that as Ni concentration increases, the Ni-t_{2g} contribution near the Fermi level

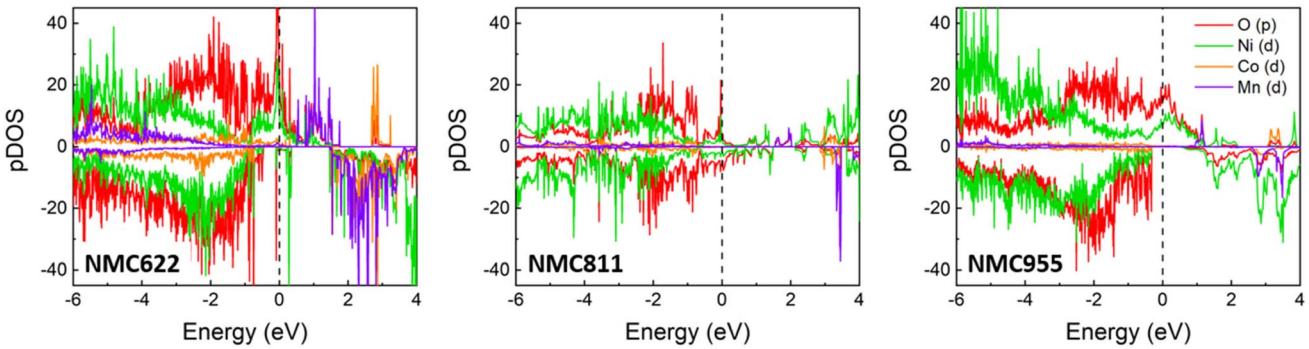

Fig. 5 Projected density of states of NMC622, NMC811, and NMC955 cathode materials at room temperature. The Fermi level indicated by the dashed lines is set to zero.

grows while the Ni-e_g band becomes partially emptied, narrowing the band gap and strengthening Ni–O hybridization. They also demonstrated that higher Ni^{4+} fractions lead to more covalent Ni–O bonds and lower oxygen-binding energies, thereby promoting oxygen release and structural degradation. Banerjee *et al.*[61] further confirmed through many-body calculations that in Ni-rich NMCs, the formal Ni oxidation state changes little upon delithiation; instead, charge compensation occurs *via* O-2p holes formed through strong Ni–O hybridization, explaining the upward shift of O-2p states toward the Fermi level. The review by Chakraborty *et al.*[62] emphasized that Ni dominates the redox process while Co facilitates charge transfer and Mn^{4+} stabilizes the structure, consistent with the minimal Co-3d and Mn-3d contributions seen here. Additionally, Schipper *et al.*[63] reported that doping Ni-rich NMCs with high-valent cations, such as Zr^{4+}, reduces Ni^{4+} formation and mitigates oxygen loss by lowering Ni–O covalency. Overall, the pDOS evolution from NMC622 → NMC811 → NMC955 reflects the central trade-off identified in these works: increasing Ni content enhances electronic conductivity and capacity *via* stronger Ni–O hybridization and oxygen redox, but simultaneously undermines structural and thermal stability by weakening metal–oxygen bonds.

Thus, to improve the structural stability of the Ni-rich NMC955 cathode, boron doping is systematically introduced by substituting a single Ni atom within the optimized structure, explicitly targeting the Ni sites labeled in Fig. S6. The structural integrity of the resulting B-doped configurations is evaluated based on their formation energies, calculated according to eqn (S1). Sites 5 and 6 display the lowest formation energies among the various B-doped configurations. However, as formation energy alone is inadequate to determine structural stability unequivocally, phonon spectral analysis is further conducted to assess dynamical stability. Site 6 is the more favorable position for boron doping, as thoroughly explained in the SI (Fig. S6). Subsequently, aluminum co-doping is systematically explored as an additional stabilization strategy. Aluminum is recognized for enhancing the long-term structural robustness of Ni-rich cathode materials.[33,34] Consequently, AlB-doped NMC955 structures (NMC955-AlB) are simulated by substituting an additional Ni atom in the previously optimized NMC955-B configuration with an Al atom. The optimal AlB-doped configuration is identified as the one with the lowest formation energy, calculated using eqn (S1) and summarized in Table S2. For comparative reference, the optimized NMC955-AlB structure is reverted to NMC955-Al by substituting the B atom back to Ni. The optimized geometric structures of both NMC955-B and NMC955-AlB are illustrated in Fig. 6. As detailed in Table 3, the substitution of smaller Al^{3+} ions for Mn^{4+} slightly contracted the lattice dimensions, enhancing the layered structure's stability, which is reflected in an increased c/a ratio with respect to the original NMC955 systems.

The AlB co-doping strategy is designed to probe the impact of aliovalent elements on charge distribution in the modified NMC955-AlB systems. Fig. 7, S8, and S9 characterize the electronic properties of these doped systems *via* PDOS and charge density difference analyses. Upon doping, the metallic character of the parent compound is preserved, as indicated by the continuous density of states across the Fermi level, implying robust electronic conductivity critical for high-rate lithium-ion battery applications. Noteworthy changes in the local electronic environment were observed: the PDOS indicates enhanced Co spin-down contributions near 2 eV and a shift in Mn spin states, particularly in the vicinity of 3 eV and 1 eV. Concomitantly, a reduction in O-2p states at the Fermi level is observed post-doping. This is consistent with suppressing oxygen participation in redox processes, a factor often associated with improved structural stability and mitigated oxygen release at high charge states.

Furthermore, CCD mapping (Fig. 8 and S10) demonstrates electron accumulation predominantly on oxygen atoms, with depletion centered around the Al, B, and Mn sites. This redistribution indicates a net charge transfer away from the dopant sites and highlights their role in modulating the local electronic structure. The observed delocalization of charge around oxygen can be interpreted as a stabilization mechanism that alleviates localized electron density, potentially suppressing the formation of reactive oxygen species. These results collectively suggest that co-doping with Al and B enhances Ni-rich layered cathodes' structural and electronic stability under electrochemical stress.

The migration of lithium ions within layered cathode lattices governs both the charge–discharge kinetics and rate

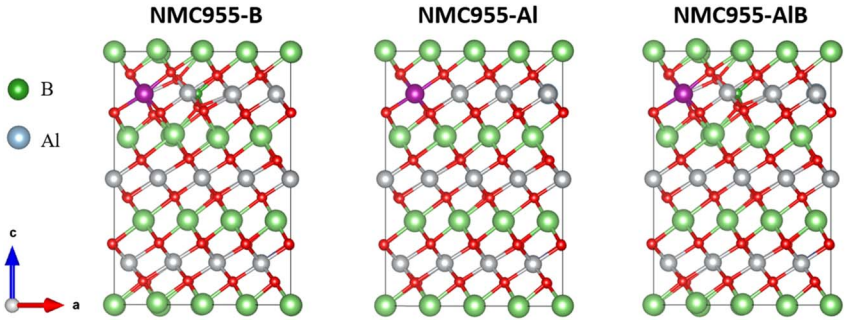

Fig. 6 Side views of the optimized NMC955-B, NMC955-Al, and NMC955-AlB cathode materials at room temperature. Green, gray, purple, blue, and red spheres represent lithium, nickel, manganese, cobalt, and oxygen atoms, respectively.

Table 3 Lattice parameters of B and Al-doped NMC955 cathode materials at room temperature

Material	a (Å)	c (Å)	c/a
NMC955-B	2.874	14.318	4.982
NMC955-Al	2.904	14.347	4.940
NMC955-AlB	2.896	14.331	4.949

performance of lithium-ion batteries. In Ni-rich layered oxides such as NMC955, lithium diffusion primarily occurs through the two-dimensional Li–O slabs parallel to the *ab*-plane. To evaluate the role of B-doping and AlB co-doping on NMC955 cathode materials, we evaluate the diffusion barrier and migration pathway *via* the climbing-image nudged elastic band method to determine the minimum energy pathways for lithium diffusion in pristine NMC955, B-doped NMC955, and Al–B co-doped NMC955 systems. The calculated migration trajectories are illustrated in Fig. 9a, with the corresponding energy profiles shown in Fig. 9b–d. The diffusion barrier for pristine NMC955 is computed to be 0.355 eV (Table 4), in close agreement with reported values of 0.30–0.40 eV for conventional NMC811 and $LiNiO_2$ cathodes,[16,29,48] indicating moderate mobility and confirming that Li-ion transport remains kinetically limited in Ni-rich compositions. Such a barrier, while thermally surmountable at room temperature, constrains high-rate charging and accentuates voltage hysteresis during cycling. The corresponding diffusion coefficient of NMC955 cathode materials of 3.2×10^{-7} cm^2 s^{-1} is much faster than the typical experimental report of NMC622 and $MoNb_{12}O_{33}$ electrodes of $\sim 10^{-9}$ cm^2 s^{-1}.[64] Remarkably, substitutional boron doping significantly reduces the diffusion barrier to 0.191 eV. This reduction arises from local lattice relaxation and electronic modulation induced by B incorporation, which expands the Li–O slab spacing and weakens the Li–O electrostatic interaction along the diffusion path. The formation of strong B–O covalent bonds further stabilizes the oxygen sublattice, mitigating oxygen release and lattice distortion during (de)lithiation.[29,55] More interestingly, upon Al and B co-doping, the migration barrier is 0.206 eV, slightly higher than that of the B-only system but still far below that of pristine NMC955. The corresponding diffusion coefficients of these doped cathode materials are even comparable to those of $LiMn_2O_4$ and $LiMn_2O_4$-MXene nanocomposite cathodes.[65] This result indicates an overall effect between the two dopants: Al substitution stabilizes the transition-metal layer and suppresses cation mixing. At the same time, B maintains expanded Li diffusion pathways and introduces charge delocalization, facilitating Li hopping. The Al–B co-doped system thus achieves a balance between structural stability and ionic conductivity, ensuring both fast diffusion and long-term phase integrity under high-voltage cycling.

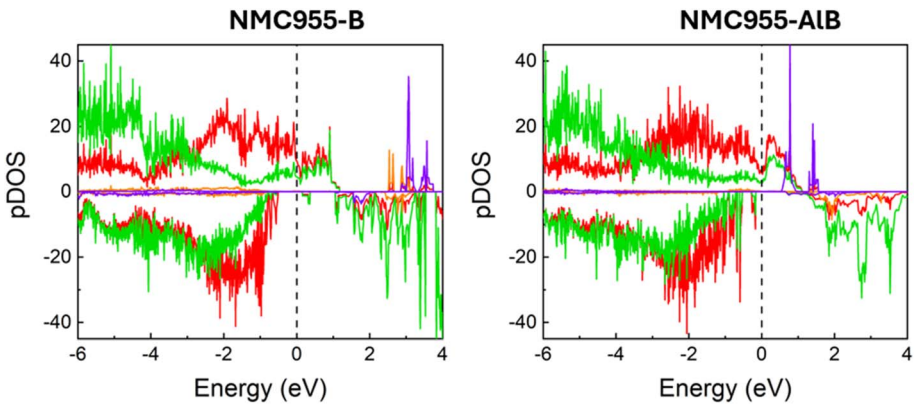

Fig. 7 Project density of states of NMC955-B and NMC955-AlB cathode materials. The Fermi level indicated by the dashed lines is set to zero.

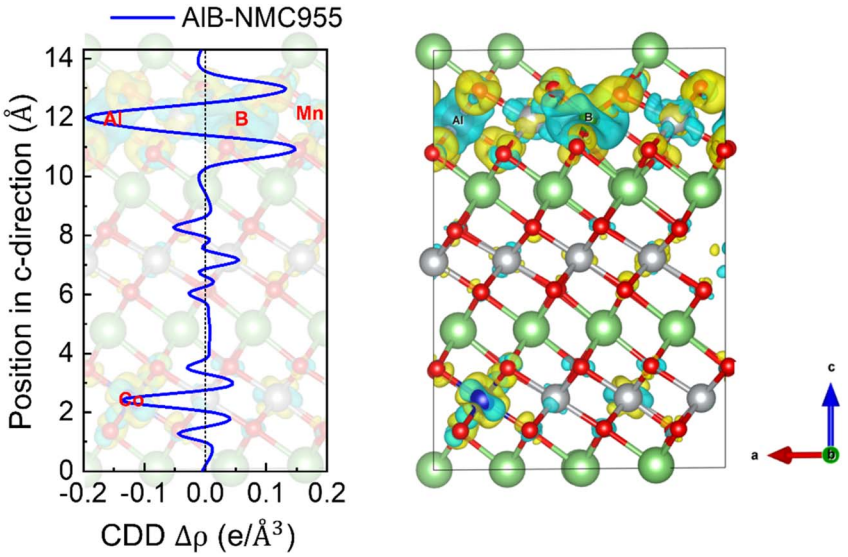

Fig. 8 The charge density difference (CDD) profiles along the *c*-direction upon codoping Al and B onto NMC955 cathode materials. The iso-surface is set at 0.005 eÅ^{-3}. The yellow iso-surface indicates areas of charge accumulation, while the cyan iso-surface represents charge depletion.

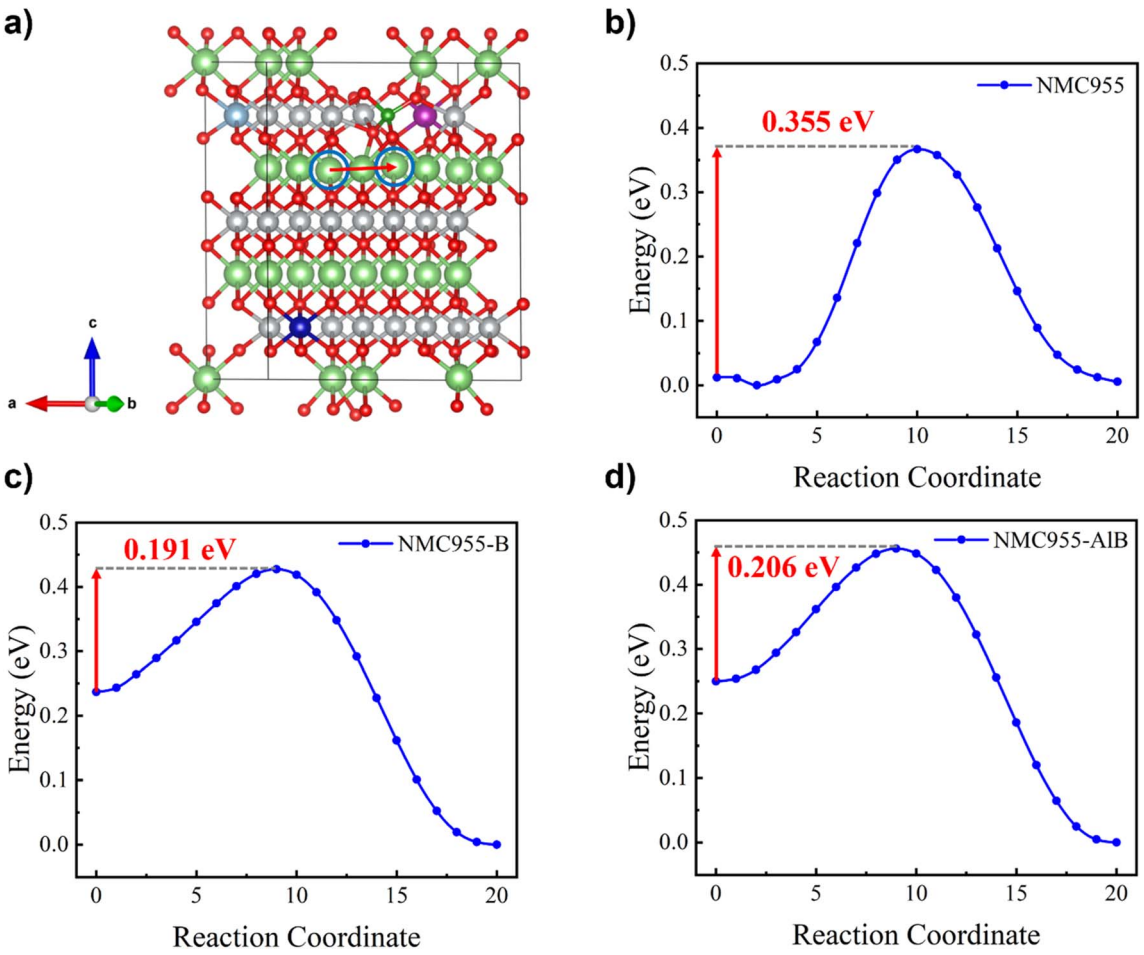

Fig. 9 Diffusion pathway of lithium-ion on AlB co-doped NMC955 cathodes (a), diffusion barriers of lithium atoms of pristine (b), B-doped (c), and AlB co-doped (d) NMC955 cathode materials.

Table 4 Diffusion barrier and diffusion coefficient of lithium ions of pristine, B-doped and AlB co-doped NMC955 cathode materials

Systems/characteristics	NMC955	B-Doped NMC955	AlB co-doped NMC955
Diffusion barrier (eV)	0.355	0.191	0.206
Diffusion coefficient ($cm^2\ s^{-1}$)	3.2×10^{-7}	8.1×10^{-5}	4.5×10^{-5}

4. Conclusion

This work combines density functional theory and machine learning to evaluate the stability and electronic behavior of Ni-rich layered cathodes. The trained DeePMD neural network models accurately reproduce DFT energies and forces ($R^2 > 0.9$), confirming their reliability for large-scale simulations. Increasing Ni content enhances electronic conductivity but weakens structural integrity through stronger Ni–O hybridization. Among the studied systems, NMC955 shows the highest conductivity yet the lowest stability. Co-doping with Al and B markedly improves lattice robustness, redistributes charge, and reduces local strain, while lowering the Li-ion diffusion barrier from 0.355 eV to 0.206 eV. The Al–B co-doping stabilizes the oxygen framework and enhances ion mobility, achieving a balance between conductivity and durability. These findings demonstrate an effective DFT-ML strategy for designing high-energy, long-life Ni-rich cathodes and guiding the development of next-generation lithium-ion batteries.

Conflicts of interest

There are no conflicts of interest to declare.

Data availability

The data supporting this article have been included as part of the supplementary information (SI). Supplementary information: results of *ab initio* molecular dynamics (AIMD) simulations (part I); details of machine-learning approach (part II); electronic properties of undoped NMC cathode materials (part III); details of doping strategies (part IV); electronic properties of Al and B doped on NMC955 cathode materials (part V). See DOI: https://doi.org/10.1039/d5ra03510d.

Acknowledgements

This research is funded by the Ministry of Education and Training, Vietnam (under Grant number B2024-TCT-16). The authors acknowledge the Information and Network Management Centre at Can Tho University for providing high-performance computing resources.

References

1 R. Amaral and N. Y. Dzade, *Appl. Surf. Sci.*, 2024, **659**, 159847.
2 E. C. Evarts, *Nature*, 2015, **526**, S93–S95.
3 J. B. Goodenough and K. Park, *J. Am. Chem. Soc.*, 2013, **135**, 1167–1176.
4 J.-H. Li, J. Wu and Y.-X. Yu, *J. Phys. Chem. C*, 2021, **125**, 3725–3732.
5 J.-H. Li, J. Wu and Y.-X. Yu, *J. Mater. Chem. A*, 2021, **9**, 10186–10198.
6 C. Erinmwingbovo, M. S. Palagonia, D. Brogioli and F. La Mantia, *ChemPhysChem*, 2017, **18**, 917–925.
7 Z.-H. Wu and Y.-X. Yu, *ACS Appl. Energy Mater.*, 2024, **7**, 8715–8725.
8 H. Yang, C. N. Savory, B. J. Morgan, D. O. Scanlon, J. M. Skelton and A. Walsh, *Chem. Mater.*, 2020, **32**, 7542–7550.
9 D. Peralta, J. Salomon, J.-F. Colin, A. Boulineau, F. Fabre, C. Bourbon, B. Amestoy, E. Gutel, D. Bloch and S. Patoux, *J. Power Sources*, 2018, **396**, 527–532.
10 R. Li, P. Zhang, J. Huang, B. Liu, M. Zhou, B. Wen, Y. Luo and S. Okada, *RSC Adv.*, 2021, **11**, 7886–7895.
11 J. Li, H. Li, W. Stone, R. Weber, S. Hy and J. R. Dahn, *J. Electrochem. Soc.*, 2017, **164**, A3529–A3537.
12 F. Aupperle, G. G. Eshetu, K. W. Eberman, A. Xioa, J. S. Bridel and E. Figgemeier, *J. Mater. Chem. A*, 2020, **8**, 19573–19587.
13 T. Le Thi, T. Phan Van, B. Nguyen Van, N. To Van, T. Nguyen Van, T. P. Doan, T. L. Ngo, N. H. Vu, T.-T. Nguyen, H. N. Nguyen, N. V. Anh Duy and M. T. Dang, *ACS Omega*, 2023, **8**, 45414–45427.
14 M. Shang, X. Chen and J. Niu, *Cell Rep. Phys. Sci.*, 2022, **3**, 100767.
15 C. Cai, D. Zhang, Q. Zhang, K. Chen, W. Hua, C. Peng and D. Xue, *J. Chem. Phys.*, 2023, **158**, 114703.
16 B. M. Gomes, M. C. Baptista, A. Orue, B. Dhrubajyoti, S. Terlicka, P. Sjövall, N. Zamperlin, C. Fonseca, J. Smajic, V. Kekkonen, W. Vonk, A. Tron, A. Schena, A. Ahniyaz and M. H. Braga, *Energy Mater.*, 2025, **5**, 500091.
17 H.-H. Sun and A. Manthiram, *Chem. Mater.*, 2017, **29**, 8486–8493.
18 H.-J. Noh, S. Youn, C. S. Yoon and Y.-K. Sun, *J. Power Sources*, 2013, **233**, 121–130.
19 Q. Wang, C. H. Shen, S. Y. Shen, Y. F. Xu, C. G. Shi, L. Huang, J. T. Li and S. G. Sun, *ACS Appl. Mater. Interfaces*, 2017, **9**, 24731–24742.
20 T. M. M. Heenan, A. Wade, C. Tan, J. E. Parker, D. Matras, A. S. Leach, J. B. Robinson, A. Llewellyn, A. Dimitrijevic, R. Jervis, P. D. Quinn, D. J. L. Brett and P. R. Shearing, *Adv. Energy Mater.*, 2020, **10**, 2002655.
21 I. A. Skvortsova, E. D. Orlova, A. O. Boev, D. A. Aksyonov, I. Moiseev, E. M. Pazhetnov, A. A. Savina and A. M. Abakumov, *J. Power Sources*, 2023, **583**, 233571.
22 H.-H. Ryu, K.-J. Park, C. S. Yoon and Y.-K. Sun, *Chem. Mater.*, 2018, **30**, 1155–1163.
23 H. J. Noh, S. Youn, C. S. Yoon and Y. K. Sun, *J. Power Sources*, 2013, **233**, 121–130.
24 F. Wu, Q. Li, L. Chen, Y. Lu, Y. Su, L. Bao, R. Chen and S. Chen, *ChemSusChem*, 2019, **12**, 935–943.

25 Z. Chen, G.-T. Kim, G. Yang, D. Bresser, T. Diemant, Y. Huang, M. Copley, R. Behm, S. Passerini and Z. Shen, *J. Power Sources*, 2018, **402**, 263–271.
26 J.-H. Shim, Y.-M. Kim, M. Park, J. Kim and S. Lee, *ACS Appl. Mater. Interfaces*, 2017, **9**, 18720–18729.
27 Y. Cao, X. Qi, K. Hu, Y. Wang, Z. Gan, Y. Li, G. Hu, Z. Peng and K. Du, *ACS Appl. Mater. Interfaces*, 2018, **10**, 18270–18280.
28 S. F. Amalraj, R. Raman, A. Chakraborty, N. Leifer, R. Nanda, S. Kunnikuruvan, T. Kravchuk, J. Grinblat, V. Ezersky, R. Sun, F. L. Deepak, C. Erk, X. Wu, S. Maiti, H. Sclar, G. Goobes, D. T. Major, M. Talianker, B. Markovsky and D. Aurbach, *Energy Storage Mater*, 2021, **42**, 594–607.
29 G. Ko, S. Jeong, S. Park, J. Lee, S. Kim, Y. Shin, W. Kim and K. Kwon, *Energy Storage Mater*, 2023, **60**, 102840.
30 H. Xie, H. Peng, D. Jiang, Z. Xiao, X. Liu, H. Liang, M. Wu, D. Liu, Y. Li, Y. Sun, S. Zhong, Z. Qian and R. Wang, *Chem. Eng. J.*, 2023, **470**, 144051.
31 K. J. Park, H. G. Jung, L. Y. Kuo, P. Kaghazchi, C. S. Yoon and Y. K. Sun, *Adv. Energy Mater.*, 2018, **8**, 1801202.
32 Z. Sun, L. Xu, C. Dong, H. Zhang, M. Zhang, Y. Liu, Y. Zhou, Y. Han and Y. Chen, *J. Mater. Chem. A*, 2019, **7**, 3375–3383.
33 Y. S. Byeon, W. Lee, S. Park, D. Kim, J. Jung, M. S. Park and W. S. Yoon, *Small Science*, 2024, **4**, 2400165.
34 Y.-C. Li, W. Xiang, Z.-G. Wu, C.-L. Xu, Y.-D. Xu, Y. Xiao, Z.-G. Yang, C.-J. Wu, G.-P. Lv and X.-D. Guo, *Electrochim. Acta*, 2018, **291**, 84–94.
35 J. Tao, Y. Cui, H. Xiao, L. Zhang, Z. Wang and Q. Huang, *Ionics*, 2024, **30**, 3863–3879.
36 Y. C. Li, W. Xiang, Z. G. Wu, C. L. Xu, Y. Di Xu, Y. Xiao, Z. G. Yang, C. J. Wu, G. P. Lv and X. D. Guo, *Electrochim. Acta*, 2018, **291**, 84–94.
37 J. Behler and M. Parrinello, *Phys. Rev. Lett.*, 2007, **98**, 146401.
38 L. Zhang, J. Han, H. Wang, R. Car and W. E, *Phys. Rev. Lett.*, 2018, **120**, 143001.
39 J. Zeng, D. Zhang, D. Lu, P. Mo, Z. Li, Y. Chen, M. Rynik, L. Huang, Z. Li, S. Shi, Y. Wang, H. Ye, P. Tuo, J. Yang, Y. Ding, Y. Li, D. Tisi, Q. Zeng, H. Bao, Y. Xia, J. Huang, K. Muraoka, Y. Wang, J. Chang, F. Yuan, S. L. Bore, C. Cai, Y. Lin, B. Wang, J. Xu, J. X. Zhu, C. Luo, Y. Zhang, R. E. A. Goodall, W. Liang, A. K. Singh, S. Yao, J. Zhang, R. Wentzcovitch, J. Han, J. Liu, W. Jia, D. M. York, E. Weinan, R. Car, L. Zhang and H. Wang, *J. Chem. Phys.*, 2023, **159**, 54801.
40 L. Zhang, J. Han, H. Wang, W. A. Saidi and R. Car, *Advances in Neural Information Processing Systems*, 2018, pp. 4436–4446.
41 D. P. Kingma and J. L. Ba, 3rd International Conference on Learning Representations, ICLR 2015 - Conference Track Proceedings, in, *Adam: A Method for Stochastic Optimization*, 2015, https://dare.uva.nl/search?identifier=a20791d3-1aff-464a-8544-268383c33a75.
42 W.-C. Fan, Z. Guan, L.-Q. Wei, H.-W. Xu, W.-Y. Tong, M. Tian, N. Wan, C.-S. Yao, J.-D. Zheng, B.-B. Chen, P.-H. Xiang, N. Zhong and C.-G. Duan, *Nat. Commun.*, 2025, **16**, 3557.
43 G. Kresse and J. Hafner, *Phys. Rev. B:Condens. Matter Mater. Phys.*, 1994, **49**, 14251.
44 G. Kresse and D. Joubert, *Phys. Rev. B:Condens. Matter Mater. Phys.*, 1999, **59**, 1758.
45 G. Kresse and J. Furthmüller, *Comput. Mater. Sci.*, 1996, **6**, 15–50.
46 J. P. Perdew, K. Burke and M. Ernzerhof, *Phys. Rev. Lett.*, 1996, **77**, 3865.
47 J. P. Perdew, A. Ruzsinszky, G. I. Csonka, O. A. Vydrov, G. E. Scuseria, L. A. Constantin, X. Zhou and K. Burke, *Phys. Rev. Lett.*, 2008, **100**, 136406.
48 H. Banerjee, C. P. Grey and A. J. Morris, *Chem. Mater.*, 2024, **36**, 6575–6587.
49 H. J. Monkhorst and J. D. Pack, *Phys. Rev. B:Condens. Matter Mater. Phys.*, 1976, **13**, 5188.
50 G. Henkelman, B. P. Uberuaga and H. Jónsson, *J. Chem. Phys.*, 2000, **113**, 9901–9904.
51 G. Henkelman and H. Jónsson, *J. Chem. Phys.*, 2000, **113**, 9978–9985.
52 T. N. Tran, N. V. Anh Duy, N. H. Hieu, T. A. Nguyen, N. T. Van, T. V. Bac Phung, Y. A. Zulueta, M. T. Nguyen, P. Schall and M. T. Dang, *RSC Adv.*, 2024, **14**, 33524–33535.
53 T. L. Nguyen, B. T. Nguyen Thi, A. D. Nguyen Vo, T. H. Nguyen Thi and M. T. Dang, *Adv. Nat. Sci.:Nanosci. Nanotechnol.*, 2025, **16**, 045008.
54 T. Le Thi, T. Phan Van, B. Nguyen Van, N. To Van, T. Nguyen Van, T. P. Doan, T. L. Ngo, N. H. Vu, T.-T. Nguyen, H. N. Nguyen, N. V. Anh Duy and M. T. Dang, *ACS Omega*, 2023, **8**, 45414–45427.
55 N. To Van, N. V. A. Duy, N. H. Hieu, Q. Q. Ngo, T. Son Luong, T. L. Ngo, Y. A. Zulueta, M. T. Nguyen, A.-G. Nguyen, P. L. Nguyen, C.-J. Park and M. T. Dang, *Dalton Trans.*, 2025, **54**, 14173–14190.
56 S. Windisch-Kern, A. Holzer, C. Ponak, T. Hochsteiner and H. Raupenstrauch, *Carbon Resour. Convers.*, 2021, **4**, 184–189.
57 S. U. D. Shamim, A. Siddique, B. K. Dash, T. Ahmed, S. Shaha, M. Islam and A. A. Piya, *Langmuir*, 2025, **41**, 8726–8739.
58 B. Schwarz, S. Mangold, H. Li, S. Indris and H. Ehrenberg, *Phys. Rev. Mater.*, 2025, **9**, 45401.
59 M. Jiang, D. L. Danilov, R.-A. Eichel and P. H. L. Notten, *Adv. Energy Mater.*, 2021, **11**, 2103005.
60 M. Dixit, B. Markovsky, F. Schipper, D. Aurbach and D. T. Major, *J. Phys. Chem. C*, 2017, **121**, 22628–22636.
61 H. Banerjee, C. P. Grey and A. J. Morris, *Chem. Mater.*, 2024, **36**, 6575–6587.
62 A. Chakraborty, S. Kunnikuruvan, S. Kumar, B. Markovsky, D. Aurbach, M. Dixit and D. T. Major, *Chem. Mater.*, 2020, **32**, 915–952.
63 F. Schipper, M. Dixit, D. Kovacheva, M. Talianker, O. Haik, J. Grinblat, E. M. Erickson, C. Ghanty, D. T. Major, B. Markovsky and D. Aurbach, *J. Mater. Chem. A*, 2016, **4**, 16073–16084.
64 Y. Lakhdar, Y. Chen, H. Geary, M. E. Houck, A. S. Groombridge, P. R. Slater and E. Kendrick, *J. Power Sources*, 2023, **588**, 233710.
65 M. E. S. Ali, H. A. Tariq, B. Moossa, Z. A. Qureshi, R. Kahraman, S. Al-Qaradawi and R. A. Shakoor, *Energy Rep.*, 2024, **11**, 2401–2414.